INTERNATIONAL JOURNAL FOR NUMERICAL METHODS IN FLUIDS
Int. J. Numer. Meth. Fluids 2008; **56**:115–141

Developing implicit pressure-weighted upwinding scheme to calculate steady and unsteady flows on unstructured grids

M. Darbandi*,†,‡ and S. Vakilipour§

Department of Aerospace Engineering, Sharif University of Technology, Tehran, P.O. Box 11365-8639, Iran

SUMMARY

The finite-volume methods normally utilize either simple or complicated mathematical expressions to interpolate the fluxes at the cell faces of their unstructured volumes. Alternatively, we benefit from the advantages of both finite-volume and finite-element methods and estimate the advection terms on the cell faces using an inclusive pressure-weighted upwinding scheme extended on unstructured grids. The present pressure-based method treats the steady and unsteady flows on a collocated grid arrangement. However, to avoid a non-physical spurious pressure field pattern, two mass flux per volume expressions are derived at the cell interfaces. The dual advantages of using an unstructured-based discretization and a pressure-weighted upwinding scheme result in obtaining high accurate solutions with noticeable progress in the performance of the primitive method extended on the structured grids. The accuracy and performance of the extended formulations are demonstrated by solving different standard and benchmark problems. The results show that there are excellent agreements with both benchmark and analytical solutions as well as experimental data. Copyright © 2007 John Wiley & Sons, Ltd.

Received 23 August 2006; Revised 15 December 2006; Accepted 18 December 2006

KEY WORDS: finite volume; finite element; unstructured grid; pressure-based algorithm; upwinding scheme; collocated grid

1. INTRODUCTION

The past two decades has shown that there has been an increasing interest in the unstructured-grid employment in finite-volume methods because it not only retains the conservation properties of the finite-volume method but also eases grid generation in complex computational domains. As it is known, local mesh refinement, either adaptive or fixed, is a major demand in the computational fluid

---

*Correspondence to: M. Darbandi, Department of Aerospace Engineering, Sharif University of Technology, Tehran, P.O. Box 11365-8639, Iran.

† E-mail: darbandi@sharif.edu

‡ Professor.

§ Ph.D. Candidate.

dynamics. This can be easily achieved *via* unstructured grid employment [1]. Generally speaking, the numerous advantages of unstructured grids have promoted the grid generation research to focus on developing more robust and more efficient unstructured grid generation techniques. Mavriplis [2] and Morgan and Peraire [3] have presented a complete overview of the basic unstructured mesh techniques for computational fluid dynamics. Few pioneering works in the unstructured grid includes that of Lohner *et al.* [4], Mavriplis [5], and Barth [6]. Following various grid generation techniques, efforts have been devoted to the development of finite-element methods capable of implementing on general unstructured grids [7, 8]. This implementation is rather straightforward. Contrary to the finite-element method, the finite-volume methods face more severe difficulties to treat them on unstructured grids. One fundamental problem with solving the incompressible equations is the velocity–pressure formulation and equal-order interpolation, presumably because of the stability difficulties associated with central difference type schemes for this class of problems. This difficulty is extensively described in this work. Another difficulty is the use of multigrid cycles on the unstructured grids [5, 9–11]. As an example, Wang and Joshi [12] employed an algebraic multigrid procedure in their cell-centred finite-volume method to solve incompressible flow. The other problem is the extension of higher-order upwind scheme on unstructured grids. Barth and Jepersen [13], Zhao and Zhang [14], and Woodfield *et al.* [15] are just few references among many, who presented high-order upwind scheme to treat the convection terms at the cell faces with or without introducing limiters and to suppress spurious oscillations around the discontinuities.

From the finite-volume perspective, the approximation of fluxes at the cell faces can be drastically improved by incorporating the correct physics of flow in the cell-face expressions. For example, a basic upwind estimation for the convection terms produces false diffusion [16]. However, the false diffusion can be decreased dramatically if upwinding is skewed in the flow direction [17]. Unfortunately, the upwinding is not the sole physics behind approximating the cell-face velocity. A more inclusive suggestion is to incorporate the weight of other key parameters in the approximation. Schneider and Raw [18] presented a mass-weighted, skewed, positive influence coefficient upwind scheme on quadrilateral mesh. Schneider and Raw [19] and Darbandi and Schneider [20] showed that the approximation could be effectively improved if the pressure was also included in the advection term approximations. In the next paragraphs, we briefly mention how different schemes treat the fluxes at the cell faces.

As was mentioned before, one major problem with treating the incompressible governing equations is the decoupling of velocity and pressure fields. The solution of the incompressible flow equations faces a particular difficulty due to the fact that the continuity equation does not directly involve the pressure term. The artificial compressibility method of Chorin [21], (e.g. [9, 14, 22]) or the limit of the compressible flow equations through preconditioning (e.g. [11, 23]) have generally employed to provide suitable links among the incompressible governing equations. These techniques overcome the aforementioned difficulty and suppress oscillatory pattern in the pressure field. For example, Jorgenson and Pletcher [23] developed a finite-volume pressure-based algorithm to solve the 2D compressible equations on unstructured grids using temporal preconditioning approach, which enabled them to solve very low Mach number flows. They applied a cell-centred scheme in their algorithm.

Another approach commonly used to alleviate the non-physical pressure pattern is a staggered arrangement of the variables, which were initially introduced by Harlow and Welch [24] on the Cartesian grids. It has led to several variations depending on the location of the variables [25]. The staggered grid arrangement is equivalent to the unequal-order interpolation for pressure and velocity, which is commonly used in the finite-element context to achieve stability as expressed by Ladyzhenskaya–Babuska–Brezzi condition. The staggered grid arrangement has been practiced in unstructured grid arrangement since many years ago. Rida *et al*. [26] used the skewed mass-weighted upwind function proposed by Schneider and Raw [18] to estimate the convection terms at the cell faces. Kobayashi *et al*. [27] employed a finite-volume discretization method to solve steady 2D incompressible flow on unstructured grids. They applied a second-order least-squares scheme for convection discretization and a fractional step projection method based on a staggered grid arrangement for pressure–velocity coupling. Vidovic *et al*. [28] developed an upwind-biased finite-volume method to treat flow on staggered triangular grids using linear reconstruction of staggered vector fields. They did not use assumption of incompressibility in the spatial discretization to allow the extension of their scheme to the compressible case. From a hybrid method perspective, Baliga and Patankar [29] solved the 2D incompressible flow using finite-volume-based finite-element method. They used a combination of six-node macroelements and three-node triangular subelements to avoid pressure velocity decoupling.

Besides suppressing the spurious pressure mode, the staggered grid employment may provide additional benefits in specific applications. For example, considering a proper choice for time advancing schemes, the staggered-based discretization conserves the global kinetic energy. Perot [30] and Zhang *et al*. [31] solved 2D and 3D laminar flows on unstructured grids and discussed the roles of discrete operators for the curl and divergence in ensuring kinetic energy conservation. This conservation made their numerical solution robust without the use of numerical dissipation. Benhamadouche and Laurence [32] and Mahesh *et al*. [33] developed a non-dissipative formulation for LES on unstructured staggered grid. They indicated that the role of discrete energy conservation had been extremely important in achieving a robust and accurate formulation. Contrary to the above benefits, there are major difficulties in employing the staggered grids to discretize complex geometries. One major difficulty is the dual bookkeeping requirement for velocity, pressure, and the other flow field variables. The problem becomes very tedious on curvilinear coordinate system [34, 35] and very complicated in unstructured grid employments [28, 30, 33]. Additionally, the classical first-order and second-order upwind schemes produce more false diffusion on general grid systems [34, 36]. There are references which extensively study the variations of staggered grid arrangements with their alternative known as collocated one [25, 37].

An alternative to staggered grid employment is the use of a dual-velocity interpolation on collocated grids. As the pioneers in the collocated scheme, Rhie and Chow [38] invented this approach and relied on averaging techniques for the coefficients of the momentum equations at the cell interfaces because the velocities were not available at the cell faces of a non-staggered grid arrangement. Additionally, the proposition of the equal-order collocated scheme of Prakash and Patankar [39] permitted the collocation of pressure and velocity at the same nodes. As a more inclusive scheme, Saabas and Baliga [40] and Masson *et al*. [41] used the upwind scheme of Schneider and Raw [18] and developed their own strategy called first-order mass-weighted upwind scheme to treat the convection terms on unstructured grids. Tran *et al*. [42] extended this scheme to a second-order upwind scheme and showed that it would improve the solution accuracy effectively. Davidson [43] presented a pressure correction procedure for the unstructured meshes using a cell-centred, collocated finite-volume method. The pressure–velocity coupling was treated using SIMPLEC. Central differencing was used for the convection terms together with fourth-order numerical dissipation and central differencing was employed for the diffusion terms. To avoid pressure–velocity decoupling, the mass flux at cell faces was computed using the Rhie and Chow interpolation. In the SIMPLE-based algorithms, the velocity field information calculated *via* the momentum equations is used to calculate the pressure field *via* the continuity equation. Lai [44] utilized a pressure-based collocated cell-centred storage scheme to solve incompressible flow on unstructured grids as well. He used an element-centre storage scheme so that all the dependent variables were located at element centres. He used the pressure implicit with splitting of operators (PISO) of Issa [45] to couple the velocity and pressure fields. Wang and Joshi [12] employed a cell-centred collocated finite-volume method to solve incompressible flow on unstructured grid. Chenier *et al.* [46] used an original method leading to local redistributions of the fluid mass, which simultaneously yielded the control of the kinetic energy and the convergence of their collocated finite-volume scheme for solving incompressible flow on unstructured grids.

Despite the aforementioned progresses of unstructured grid employment in the finite-volume methods, there is still demand in more robust schemes capable of achieving higher accuracy and performance in engineering flow analysis. Similarly, we also extend a novel pressure-weighted upwinding scheme to unstructured collocated grid employments. The current scheme implements the physics of flow field accurately in modelling the advection terms at the cell interfaces. Additionally, the influence of pressure field is also included in treating the mass fluxes in the continuity equation in order to create a suitable coupling between pressure and velocity fields. The important features of this approach can be counted as the use of a velocity–pressure formulation with equal-order interpolation and the computation of the flow field *via* an implicit procedure. The method by which this can be achieved has already been successfully demonstrated in the case of steady flow on structured quadrilateral [20, 47], triangular [48], and hybrid [49] grids. In the present work, we further extend the proposed upwinding strategy to steady and unsteady flows on unstructured grid.

2. THE GOVERNING EQUATIONS

The 2D conservation laws for mass, momentum, and energy without any source terms are given by

$$\frac{\partial\psi}{\partial t}+\frac{\partial A(\psi)}{\partial x}+\frac{\partial B(\psi)}{\partial y}=\frac{\partial C(\psi)}{\partial x}+\frac{\partial D(\psi)}{\partial y} \tag{1}$$

where the solution vector ψ, convection vectors (A and B), and diffusion vectors (C and D) are defined as

$$[\psi\ \ A\ \ B\ \ C\ \ D]=\begin{bmatrix} \rho & \rho u & \rho v & 0 & 0 \\ \rho u & \rho uu+p & \rho vu & \tau_{xx} & \tau_{yx} \\ \rho v & \rho uv & \rho vv+p & \tau_{xy} & \tau_{yy} \\ \rho e & \rho uh & \rho vh & u\tau_{xx}+v\tau_{xy}-q_x & u\tau_{yx}+v\tau_{yy}-q_y \end{bmatrix} \tag{2}$$

where u, v, ρ, p, e, and h represent the longitudinal and transversal velocities, density, pressure, total specific energy, and the total enthalpy, respectively. The Newtonian fluid assumption is used to present the stress tensor components. The assumption leads to

$$\tau_{xx}=2\mu\frac{\partial u}{\partial x}-\left\{\frac{2}{3}\mu\left(\frac{\partial u}{\partial x}+\frac{\partial v}{\partial y}\right)\right\} \tag{3}$$

$$\tau_{xy}=\tau_{yx}=\mu\left(\frac{\partial u}{\partial y}+\frac{\partial v}{\partial x}\right),\quad \tau_{yy}=2\mu\frac{\partial v}{\partial y}-\left\{\frac{2}{3}\mu\left(\frac{\partial u}{\partial x}+\frac{\partial v}{\partial y}\right)\right\} \tag{4}$$

where μ represents the molecular viscosity coefficient. The terms inside the braces in Equations (3) and (4) vanish in incompressible limit. Using the Fourier's law in heat conduction and assuming negligible potential energy, the heat fluxes and the total enthalpy are calculated from

$$q_x=-k\frac{\partial T}{\partial x},\quad q_y=-k\frac{\partial T}{\partial y} \tag{5}$$

$$h=c_pT+(u^2+v^2)/2 \tag{6}$$

where T, k, c_p represent the temperature, thermal conductivity coefficient, and the specific heat at constant pressure, respectively. The governing equations are numerically treated in the next sections using the advantages of both finite-volume and finite-element methods.

3. THE UNSTRUCTURED DISCRETIZATION APPROACH

The computational domain is broken into an unstructured assembly of triangular elements. We achieve this discretization, for domains of arbitrary geometrical complexity, by employing the grid generator described by Reference [1]. It uses the advancing front method to triangulate the computational boundaries and to create the triangles within the computational domain. User-specified grid parameter distribution functions are used to control the shape and size of the generated elements. The Delaunay criterion enforces that no other point in the computational domain lies within the circumcircle of a given triangle element. Moreover, a mesh refinement algorithm is eventually used to improve the quality of the elements by controlling the elements aspect ratio and the maximum angle in each triangle.

Figure 1 shows a part of our generated unstructured grid in the solution domain. It consists of several triangular elements. In our finite-element approach, nodes are located at the element vertices, see the solid circles. The proper assemblage of the discrete cell faces around each individual node can create a confined region around that node, which can be used later for employing the conservation laws. The shaded area around node P in Figure 1 illustrates a discrete finite volume. However, to generate our cell, each element is broken into three sub-control-volumes (SCVs) using the medians of each triangle. The dashed lines are medians, which represent the cell faces as well. The three SCVs in each element are called SCV1, SCV2, and SCV3, see element KMS. After constructing the three SCVs in each element, three cell faces are available in each element. The fluxes through each of these three faces are approximated at their midpoints, which are named integration points; see $ip1$ and $ip2$ in SPR element. However, normal direction to each cell face is needed for integration purposes. In this regard, we define normal outward vector to each cell face. Its magnitude is equal to the cell face area and it is placed at integration point, see $\Delta S1$ and $\Delta S2$ normal vectors in element SPR. Considering SCVi in element PTQ, only the fluxes which pass through the inner surfaces of SCVi, i.e. $S1i$ and $S2i$, are needed to be integrated for the calculation of convection and diffusion fluxes. In another words, we need calculating the fluxes only at integration points of the interior faces. However, the unknowns at the integration points cannot be considered as the major unknowns in our formulation because the number of unknowns exceeds the number of available algebraic equations for the entire cells in the domain. Therefore,

DOI: 10.1002/fld

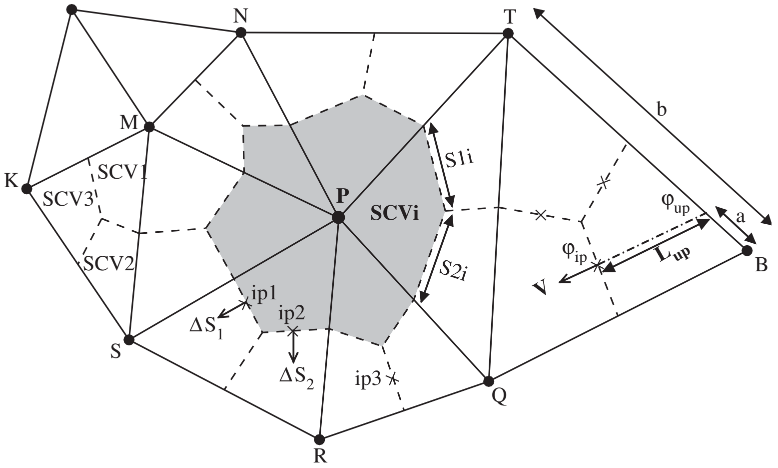

Figure 1. Grid terminology and upwinding strategy.

the variables at integration points must be presented in terms of nodal unknowns in order to be able to close the set of linear algebraic equations consistently.

The present method is pressure based and considers the pressure variable as a dependent variable in its algorithm. Almost all of the primitive pressured-based algorithms have chosen the velocity components, i.e. U and V, as their major unknowns variables [14, 41–44]. Alternatively, we have chosen the momentum components, i.e. $F=\rho U$ and $G=\rho V$, as the major unknowns in our formulation. There are a few reasons behind this decision. Since this study is a general research, which ultimately intends to develop an all-speed flow formulation and a general incompressible–compressible algorithm, this choice permits to extend our current algorithm to an all-speed flow solver [20, 47, 50, 51]. Additionally, it reduces the linearization task remarkably [50, 52]. Moreover, the momentum variables are constant passing through a discontinuity; hence, there would be less chance for the momentum components to oscillate around discontinuities [50, 52, 53].

4. THE NUMERICAL MODELLING

Using the advantages of divergence theorem, Equation (1) is integrated over an arbitrary sub-control-volume, i.e. SCVi. Back to Figure 1 and description provided in Section 3, the convection and diffusion fluxes are integrated over only the inner faces. This consideration yields

$$\int_{\delta\upsilon_i} \frac{\partial\psi}{\partial t}\,\mathrm{d}\upsilon + \int_{S1i+S2i} (A\hat{i}+B\hat{j})\cdot\mathbf{ds} = \int_{S1i+S2i} (C\hat{i}+D\hat{j})\cdot\mathbf{ds} \tag{7}$$

where $\delta\upsilon_i$ is the volume of SCVi, **ds** is the normal outward vector to the cell face, and the parameters $S1i$ and $S2i$ indicate the two inner cell faces in conjunction with SCVi, see element PQT in Figure 1. In the present approach, the fluxes at the SCV surfaces are assumed to be uniform. Therefore, the total flux magnitude is calculated on each cell face and is placed at its integration point. For example, the calculation of the mass fluxes at integration points and their substitutions in Equation (7) finally yield

$$[a^{pfm}]\{f\}+[a^{pgm}]\{g\}=0 \tag{8}$$

To make the set of our algebraic equations more stiff, we have assumed that the flow Mach number would be very low in which the variation of density field would certainly become negligible. Therefore, to magnify this assumption, the time variation term is totally removed from Equation (8). More details of deriving Equation (8) are provided in treating the x-momentum equation. Equation (8) is in matrix form and presents three mass conservations for three SCVs in each element. Therefore, the matrices are 3×3. The vectors shown by lowercase letters, i.e. $\{f\}$ and $\{g\}$, represent f and g variables at the three integration points located within an element. We will show that they need to be presented in terms of nodal variables. The superscripts over the matrix coefficients from left to right are the name of the equation (e.g. p for the continuity equation), the name of its multiplier (e.g. f if it is multiplied by f), and the type of term (m for the mass flux, c for the convection flux, and d for the diffusion flux terms), respectively. The coefficients of matrices in Equation (8) are obtained from

$$a_{ij}^{pfm}=\begin{cases}(\Delta S_x)_{S1i} & \text{if } j=S1i\\ (\Delta S_x)_{S2i} & \text{if } j=S2i\\ 0 & \text{else}\end{cases}\qquad a_{ij}^{pgm}=\begin{cases}(\Delta S_y)_{S1i} & \text{if } j=S1i\\ (\Delta S_y)_{S2i} & \text{if } j=S2i\\ 0 & \text{else}\end{cases} \tag{9}$$

where the index i denotes the SCV number and index j denotes the integration point number. If $\mathbf{ds}=\Delta S_x\hat{\imath}+\Delta S_y\hat{\jmath}$, ΔS_x and ΔS_y are the x and y components of the normal vector to the cell face, respectively. As was mentioned before, the length of the normal vector is equal to the area of the cell face.

Similar to the continuity equation, the momentum equations can be treated and approximated at the cell faces. For example if we start from Equation (7), the x-momentum equation can be integrated over $S1i$ and $S2i$ faces of SCVi. The integration yields

$$\int_{\delta\upsilon_i}\frac{\partial(\rho u)}{\partial t}\,\mathrm{d}\upsilon+\int_{S1i+S2i}[(\rho uu+p-\tau_{xx})\hat{\imath}+(\rho vu-\tau_{yx})\hat{\jmath}]\cdot\mathbf{ds}=0 \tag{10}$$

As is observed, the convection terms are nonlinear with respect to the chosen dependent variables, i.e. P, F (or $f=\rho u$) and G (or $g=\rho v$). Therefore, the linearization of the nonlinear convection terms is mandatory and should be carefully fulfilled at this stage. Darbandi and Mokarizadeh [54] and Darbandi *et al.* [55] perform a 1D study and present different linearization strategies to linearize the convection terms with respect to the momentum variables. Their strategies are important if the flow is highly compressible. In this work, we are mainly concentrated on incompressible limit solutions, hence, we use simple linearization scheme in our formulation. Considering a simple linearization scheme, ρuu term is linearized to

$$\rho uu\approx\bar{u}(\rho u)=\bar{u}f \tag{11}$$

In this study, the bar over a variable means that it is approximated using the known magnitudes of the previous iteration in our fully implicit iterative procedure. Considering the above

DOI: 10.1002/fld

simple linearization strategy, the integrations over the two cell faces can be suitably replaced with summations on discrete faces. The result for SCVi is given by

$$(\Delta v_i/\Delta t)F+\sum_{k=1}^{2}[(\bar{u}f+p-\tau_{xx})\Delta S_x+(\bar{v}f-\tau_{yx})\Delta S_y]_{Ski}=(\Delta v_i/\Delta t)F^{\mathrm{o}} \tag{12}$$

where Δt is the time step, the superscript $^{\mathrm{o}}$ denotes the old magnitude, and k counts $S1i$ and $S2i$ cell faces of SCVi. The above transient term treatment shows that the accuracy in time would be first order in treating unsteady flow problems. The stress terms in Equation (12) can be readily discretized using the finite-element interpolations. In another words, they are directly connected to the nodal variables using the finite-element shape functions N. For example, the gradient of an arbitrary scalar such as ϕ can be approximated by

$$\frac{\partial\phi}{\partial x}=\sum_{j=1}^{3}\frac{\partial N_j}{\partial x}\Phi_j \tag{13}$$

where the uppercase letters (such as Φ) denote the magnitudes at the grid points or element vertices. In fact, Equation (13) indicates that the gradient of each arbitrary variable such as ϕ at the cell face can be evaluated by making use of the local nature of the finite-element shape functions. Considering the definitions of stress tensor terms given in Equations (3)–(4), the diffusion terms in Equation (12) need to be linearized with respect to F and G, which are our major unknowns. For example, using the definitions of $f=\rho u$ and $g=\rho v$ and their substitutions in Equation (3), τ_{xx} term can be linearized to

$$\tau_{xx}=\frac{2\mu}{3\bar{\rho}}\left[\left(2\frac{\partial f}{\partial x}-2\bar{u}\frac{\partial\bar{\rho}}{\partial x}\right)-\left(\frac{\partial g}{\partial y}-\bar{v}\frac{\partial\bar{\rho}}{\partial y}\right)\right] \tag{14}$$

As it is seen, τ_{xx} term is initially linearized to $\partial f/\partial x$ and $\partial g/\partial y$ gradient terms. We use the approximation given in Equation (13) to replace the terms in Equation (14). It eventually yields

$$\tau_{xx}\approx\frac{2\mu}{3\bar{\rho}}\left[\sum_{j=1}^{3}\left(2\frac{\partial N_j}{\partial x}F_j-\frac{\partial N_j}{\partial y}G_j\right)-\sum_{j=1}^{3}\left(2\bar{u}\frac{\partial N_j}{\partial x}-\bar{v}\frac{\partial N_j}{\partial y}\right)\bar{\tilde{\rho}}_j\right] \tag{15}$$

where $\tilde{\rho}$ is the magnitude of density at the vertices of each element. The other stress term τ_{yx} can be treated in a similar manner. The substitutions of τ_{xx} and τ_{yx} in Equation (12) and a suitable combination of similar coefficients eventually yield

$$[A^{ffd}]\{F\}+[A^{fgd}]\{G\}+[a^{ffc}]\{f\}+[a^{fpp}]\{p\}=\{A^{fd}\} \tag{16}$$

The variables in the brackets represent 3×3 matrices. Very similar to Equation (8), Equation (16) presents three x momentum conservations for the three SCVs located in an element. For example, the coefficients in the first row of the matrices represent a part of the x-momentum conservation on the cell faces of SCV1. Contrary to the matrices in Equation (8), the matrices in Equation (16) are multiplied by both the unknowns at the integration points (i.e. f and p) and the unknowns at the main grid points (i.e. F and G). To emphasize this, the matrices which are multiplied by the magnitudes at the element vertices are shown by the uppercase letter of A and at the integration points by the lowercase letter of a. Considering this point, $\{F\}$ indicates the three unknowns at the element vertices while $\{f\}$ denotes the three momentum component variables at the mid-cell faces in one element. The elements of matrices in Equation (16) are given by

$$A_{ij}^{ffd} = -\sum_{k=1}^{2}\left[\frac{4\mu}{3\bar{\rho}}\frac{\partial N_j}{\partial x}(\Delta S_x) + \frac{\mu}{\bar{\rho}}\frac{\partial N_j}{\partial y}(\Delta S_y)\right]_{Ski} + \frac{\Delta \upsilon_i}{\Delta t} \tag{17}$$

$$A_{ij}^{fgd} = -\sum_{k=1}^{2}\left[-\frac{2\mu}{3\bar{\rho}}\frac{\partial N_j}{\partial y}(\Delta S_x) + \frac{\mu}{\bar{\rho}}\frac{\partial N_j}{\partial x}(\Delta S_y)\right]_{Ski} \tag{18}$$

$$a_{ij}^{ffc} = \begin{cases} [\bar{u}(\Delta S_x) + \bar{v}(\Delta S_x)]_{S1i} & \text{if } j = S1i \\ [\bar{u}(\Delta S_x) + \bar{v}(\Delta S_x)]_{S2i} & \text{if } j = S2i \\ 0 & \text{else} \end{cases} \tag{19}$$

$$a_{ij}^{fpp} = a_{ij}^{pfm} \tag{20}$$

The right-hand-side vector in Equation (16) is given by

$$A_i^{fd} = \sum_{j=1}^{3}\sum_{k=1}^{2}\left(-\frac{4\mu}{3\bar{\rho}}\bar{u}\frac{\partial N_j}{\partial x}\bar{\tilde{\rho}}_j + \frac{2\mu}{3\bar{\rho}}\bar{v}\frac{\partial N_j}{\partial y}\bar{\tilde{\rho}}_j - \frac{\mu}{\bar{\rho}}\bar{u}\frac{\partial N_j}{\partial y}\bar{\tilde{\rho}}_j - \frac{\mu}{\bar{\rho}}\bar{v}\frac{\partial N_j}{\partial x}\bar{\tilde{\rho}}_j\right)_{Ski} + \frac{\Delta \upsilon_i}{\Delta t}F^{\mathrm{o}} \tag{21}$$

If we repeat the procedure provided for treating the x-momentum similarly for the y-momentum equation, three y-momentum conservations are obtained for the three SCVs within each element. Similar to Equation (16), it eventually yields

$$[A^{gfd}]\{F\} + [A^{ggd}]\{G\} + [a^{ggc}]\{g\} + [a^{gpp}]\{p\} = \{A^{gd}\} \tag{22}$$

The matrix coefficients in this equation can be easily obtained using the strategy described for the x-momentum equation.

At this stage, we have used an assembly of finite-volume and finite-element methods to integrate the Navier–Stokes equations over the three cell faces in an arbitrary element. The next stage is to remove the ambiguity behind the unacceptable presence of the integration point unknowns in our conservative statements, i.e. Equations (8), (16), and (22).

5. INTEGRATION POINT EXPRESSIONS

Since $\{f\}$, $\{g\}$, and $\{p\}$ vectors appeared in Equations (8), (16), and (22) represent unknown magnitudes at the integration points, we need to develop suitable relations between integration and nodal points in order to construct a well-posed set of linear algebraic equations. Among the convection, diffusion, and pressure terms, the convection terms are the most complex. This is why we mostly focus on modelling the convection terms in this section. Since, the convection role is to transport a property in the solution domain, upwind-based schemes are recommended to model it. However, upwind-biased schemes are prone to produce false diffusion. Considering the essence of streamwise upwinding [17, 18, 42], a suitable magnitude for the unknown ϕ at an integration point can be suggested as $\phi_{ip} = \phi_{\mathrm{up}} + \Delta\phi_{ip}$, where $\Delta\phi_{ip}$ represents the variation of ϕ_{ip} in the streamwise direction. To provide an inclusive approximation for $\Delta\phi_{ip}$, the steady momentum equations are written in the streamwise direction. They yield

$$V_{\text{tot}}\frac{\partial f}{\partial s}-\mu\nabla^2 u+\frac{\partial p}{\partial x}=S^x_{\text{diff}} \tag{23}$$

$$V_{\text{tot}}\frac{\partial g}{\partial s}-\mu\nabla^2 v+\frac{\partial p}{\partial y}=S^y_{\text{diff}} \tag{24}$$

where $V_{\text{tot}}=(\bar{u}^2+\bar{v}^2)^{1/2}$ and s represents the streamwise direction. The magnitudes of $\bar{u}$ and $\bar{v}$ are approximated from the known magnitudes of the preceding iteration using their definitions, $\bar{u}=\bar{f}/\rho$ and $\bar{v}=\bar{g}/\rho$. The rest of terms in the two momentum equations are treated as source terms and taken to their right-hand sides.

Equations (23)–(24) are used to approximate f and g. Considering element QTB in Figure 1 and the direction of $\mathbf{V}$ at the mid cell face, the streamline intersects the edge BT at 'up' point. Hence, an upwind magnitude for ϕ_{ip} becomes ϕ_{up}. The distance between the integration point and its upwind point is called upwind length and is denoted by L_{up}. Considering this definition, $\partial f/\partial s$ in Equation (23) can be discretized along the streamwise direction using a backward differencing scheme. It yields

$$\left(V_{\text{tot}}\frac{\partial f}{\partial s}\right)_{ipi}\approx\left(V_{\text{tot}}\frac{f-f_{\text{up}}}{L_{\text{up}}}\right)_{ipi} \tag{25}$$

where ipi denotes the ith integration point within an element. Considering edge BT of element QBT in Figure 1, f_{up} can be calculated from

$$(f_{\text{up}})_{ipi}=\left[\frac{a}{b}F_{\text{upr}}+\left(1-\frac{a}{b}\right)F_{\text{upl}}\right]_{ipi} \tag{26}$$

where the subscripts upr and upl denote the magnitude of F at the right and left nodes to the upwind point. For the pressure term given in Equation (23), we use the approximation given in Equation (13). For the diffusion term, we use $(\nabla^2 u)_{ipi}=[(\sum_{j=1}^{3}N_jU_j-u_{ip})/L_{\text{diff}}]_{ipi}$ where L_{diff} denotes a characteristic diffusion length [20]. Since $\nabla^2 u$ is nonlinear with respect to our chosen dependent variables, we linearize it to $\nabla^2 u=(\nabla^2 f)/\rho-(u\nabla^2\rho)/\rho$, which becomes $\nabla^2 u=(\nabla^2 f)/\rho$ in incompressible limit.

If these two recent approximations and those given in Equations (25)–(26) are substituted in Equation (23), we can derive an expression for f_{ip} in terms of F and P magnitudes at the vertices of the element, which includes f_{ip}. After a suitable rearrangement of the derived statement, we obtain

$$\{f\}=[C^{ff}]\{F\}+[C^{fp}]\{P\}+\{C^f\} \tag{27}$$

Starting from Equation (24), a similar procedure can be repeated to approximate g at an arbitrary integration point. A suitable treatment of this equation can provide an inclusive expression for g, which is finally given by

$$\{g\}=[C^{gg}]\{G\}+[C^{gp}]\{P\}+\{C^g\} \tag{28}$$

where C^{**} and C^{*} represent 3×3 and 3×1 matrices and arrays, respectively. The superscripts have definitions very similar to those in Equation (8). Since the role of pressure variable appears in our cell-face expressions, we call them pressure-weighted upwinding. Darbandi and Schneider [56] have further extended Equations (27)–(28) to include the role of temperature field in the cell-face expression to treat buoyant flows on structured quadrilateral grids. This is out of concern in the current work.

If the cell-face expressions given by Equations (27)–(28) are substituted into the conservative statements for the continuity, i.e. Equation (8), and momentum equations, i.e. Equations (16) and (22), and we use a bilinear interpolation to approximate the pressure at integration point in those statements, the statements become only in terms of unknowns at the cell centres, hence, the set of linear algebraic equations becomes well posed. However, at this stage, we are faced with a fundamental difficulty in numerical treatment of the Navier–Stokes equations in incompressible limit. As was mentioned in the Introduction section, a stable finite-element discretization of the velocity–pressure formulation of incompressible Navier–Stokes equations requires different representation of velocity and pressure fields. In particular, C^0-interpolation generates parasitic pressures. These elements do not satisfy the inf–sup condition of Babuska and Brezzi, as discussed in [57, 58]. To treat this, various mixed finite-element approximations have been developed [59]. For example, using a velocity decomposition least-squares method, Fernandez and Hafez [60] provide a stable solution of 2D incompressible flows on linear triangular elements.

Similarly, the use of same velocity expressions in both the derived continuity and momentum equations can result in a checkerboard problem [61, 62]. As was described in the Introduction section, one primitive strategy to overcome this difficulty has been to treat the governing equations on a staggered grid. To treat the equations on a collocated grid, Rhie and Chow [38] suggested the use of two types of velocity components at the cell faces to overcome the problem. In this regard, the velocity components in the Navier–Stokes equations are categorized into convected and convecting types, in order to provide the required coupling between the velocity and pressure fields [38, 39, 43, 44, 50, 62]. All the velocities in the continuity equation are convected type, but the velocities in the momentum equations can be regarded as both types. Similar to Rhie and Chow and the rest of researchers in this field, we also need to derive additional f and g expressions, instead of u and v expressions, at the cell faces of our collocated grid because our major dependent variables are the momentum components instead of the velocity ones. In our past research, we developed expressions to treat flow on the structured quadrilateral grids [20, 47]. In the present work, we benefit from the general convecting expression suggested in 1D form by Reference [62] to derive our 2D convecting components. The additional f and g expressions are derived from the proper assemblage of the continuity and momentum equations. The new statements are defined as

$$\left(u\frac{\partial f}{\partial x}+v\frac{\partial f}{\partial y}-\mu\nabla^2 u+\frac{\partial p}{\partial x}\right)-u\left(\frac{\partial f}{\partial x}+\frac{\partial g}{\partial y}\right)=\text{the rest of terms} \tag{29}$$

$$\left(u\frac{\partial g}{\partial x}+v\frac{\partial g}{\partial y}-\mu\nabla^2 v+\frac{\partial p}{\partial y}\right)-v\left(\frac{\partial f}{\partial x}+\frac{\partial g}{\partial y}\right)=\text{the rest of terms} \tag{30}$$

Here is a strong physical interpretation behind the above equations. Since the second momentum components are needed to be substituted in the continuity equation, we somehow need to include the role of continuity equation in approximating ρu and ρv fluxes at the cell faces. However, back to the origins of f and g expressions, i.e. Equations (23)–(24), there is no direct influence of the continuity equation in deriving the first set of cell-face expressions, i.e. Equations (27)–(28). In fact, they were derived solely from the pure momentum balances. However, Equations (29)–(30) enforce direct influence of the mass balance in deriving a second set of cell-face momentum expressions, which are going to be substituted in the continuity equation, i.e. Equation (8). Therefore, if there is no spurious or non-physical solution in the computational domain, the continuity equation error given in the second set of parenthesis in Equations (29)–(30) vanishes and Equations (29)–(30) reduce to Equations (23)–(24). In another words, the current formulation is smart and uses the second momentum components wherever and whenever there is a demand.

The discretization of Equations (29)–(30) is very similar to the momentum equations given in Equations (23)–(24). There are additional gradient terms in Equations (29)–(30), which are treated using the tactic introduced in Equation (13). Since we have both $\partial f/\partial x$ and $\partial g/\partial y$ gradient terms in both Equation (29) and Equation (30), the roles of both F and G unknown variables will appear in the new cell-face expressions for f and g. After some mathematical efforts, two new statements for the cell-face velocities are obtained. They are shown by $\hat{f}$ and $\hat{g}$ and given by

$$\{\hat{f}\}=[C^{\hat{f}f}]\{F\}+[C^{\hat{f}g}]\{G\}+[C^{\hat{f}p}]\{P\}+\{C^{\hat{f}}\} \tag{31}$$

$$\{\hat{g}\}=[C^{\hat{g}f}]\{F\}+[C^{\hat{g}g}]\{G\}+[C^{\hat{g}p}]\{P\}+\{C^{\hat{g}}\} \tag{32}$$

To distinguish the new $\{\hat{f}\}$ and $\{\hat{g}\}$ from those in Equations (27)–(28), they are identified by a hat. Similar to Equations (27)–(28), these expressions are also pressure oriented, hence, they are pressure weighted as before. The new statements are substituted in $\{f\}$ and $\{g\}$ in Equation (8). This substitution ends the numerical treatment of the conservative governing equations. The next step is to assemble the constructed element stiffness matrices into the global matrix. However, implementing implicit solvers on unstructured grid arrangements is very tedious. In the next section, we explain the data structure used in the current unstructured grid approach. Before closing this section, it is necessary to describe a few points about the current method.

Considering the descriptions given on discretizing Equations (23)–(24) and Equations (29)–(30), it is clear that the current cell-face expressions are first order in velocity field calculation and second order in pressure field calculation. It is because the velocity field is upwinded while the pressure field is treated using a bilinear interpolation. However, the current cell-face approximation will be second order in both the velocity and pressure fields if the role of convection term in Equations (23)–(24), (29)–(30) becomes negligible. This condition will arise if the flow Reynolds number is sufficiently low.

Although the current formulations can be equally applied to solve either compressible or incompressible flows, our main concern in this study has been incompressible and low Mach compressible flows. As it is known, the shock capturing techniques cannot be readily extended to solve low Mach compressible and incompressible flows. We show that the current method performs no limit in treating such flows. Indeed, our experience has shown that a similar formulation has been capable of solving high-speed flow on structured quadrilateral grids. Despite using any types of limiter and/or damping functions, our results showed that the current formulation would exhibit neither undershoots and overshoots around the steep gradients nor oscillations around discontinuities [47, 52–55]. Such exhibition is normal because the derived cell-face expressions are categorized as first order. However, in spite of using first-order expressions, the investigation performed in the above references indicates that their similar first-order formulations slightly dissipates the solution around discontinuities. This can be counted as a major promotion to develop the current formulation on unstructured grid employment.

6. THE DATA STRUCTURE

For an unstructured grid approach, the design of a data structure is very important. Contrary to the work of Barth [6] and many other workers who employ an edge data structure, we consider an element-based data structure. Back to Section 3, using this structure, each node in the grid is numbered and the grid is defined by the elements and the three nodes located on the vertices of each element. We have used a loop over all elements. Therefore, the element-based data storage is used here because it is natural to the element-centred storage scheme. With element-based data, connectivity integer arrays need to be created to address mesh relations from one element to its neighbouring elements.

As was described before, the current code is basically a finite-volume-based finite-element method and consequently, an unstructured element arrangement makes the global stiffness matrix significantly sparse. The data structure required by the current sparse matrix solver includes the total number of nodes and elements and their numberings, the total number of boundary elements and nodes and their numberings, and a connectivity array. As was mentioned earlier, a connectivity array must be generated for an unstructured grid so that a cell neighbourhood is completely defined for the solver. Indeed, the connectivity arrays determine the non-zero elements in the global stiffness matrix. However, to find the number of non-zero elements and their row and column numbers inside the global stiffness matrix, the solver initially searches the grid to find the neighbouring nodes around each individual node. Eventually, three arrays whose dimensions are equal to the number of non-zero elements are constructed. They provide the row number, the column number, and the magnitude of the non-zero element in the global stiffness matrix. Providing this information, the connectivity array can be readily constructed.

The linear algebraic solver used in this research is a sparse matrix solver. It solves the set of algebraic equations using suitable assembly of direct and iterative methods. At first, it uses an LU factorization of the coefficient matrix. Secondly, the solution of linear system is found using an algorithm based on the Markowitz strategy, which utilizes pivoting to reduce fill-in while maintaining numerical stability. It can finally compute the solution of the linear algebraic equations using forward and backward substitutions [63]. Alternatively, Darbandi *et al.* [64] have used different combinations of KSP methods and preconditioners to solve the set of equations resulted from treating the incompressible flow on the structured quadrilateral grids. Their conclusion is that the GMRES can be considered as the most efficient and successful method, specifically, if it is combined with ILU preconditioner or other preconditioners, which use ILU in different blocks, such as block Jacobi or additive Schwarz. In another work, Darbandi and Banaeizadeh [65] solved the resulting sparse matrices in two ways either fully coupled or semi-coupled to improve the efficiency of solving the system of equations that resulted from the structured quadrilateral grids. The performance of the solvers was then investigated on a distributed computing environment. The study showed that a fully coupled algorithm would still perform higher capabilities on parallel machines in comparison with the segregated algorithm. In another words, although the solution time required for each iteration reduces by a factor of 6 from a fully coupled algorithm to a semi-coupled one, the need for implementing a relaxation parameter in the semi-coupled algorithm increases its total run-time.

There might be a concern whether the extension and implementation of the current 2D work to 3D applications would be very complex and time consuming. In fact, the complexity in formulation will be doubled from 2D to 3D. However, the implementation is very straightforward and it can be easily fulfilled. The most complex part can be the physical upwinding procedure, which should

DOI: 10.1002/fld

be simplified using 3D finite-element shape functions. On the other hand, the time-consuming issue can be regarded as a negative point in using the current fully implicit approach. As it was mentioned earlier, the most tedious part of the current calculations returns to the solution of the generated global sparse matrix. In 3D applications, the size of matrix and its sparseness increase very rapidly. As is known, the solution of large size matrices even in sparse form is rather a very time-consuming task. For this reason, the current workers have already started a few other ways to overcome this shortcoming. A few of these remedies can be counted as using parallel processing algorithm and parallel computations [65, 66], breaking the computational domain into a suitable assembly of sub-domains or blocks [49], switching from a fully coupled algorithm to a semi-coupled one [65], investigating Krylov subspace methods as a more efficient matrix solver [64], and so on. The undertaken research is very promising and an efficient 3D extension of the current work will be achieved in the near future.

7. THE RESULTS AND DISCUSSION

The current method is tested on unstructured grid using different standard and benchmark test cases. The first test case is the Taylor problem to study the temporal and spatial accuracy of the present formulations. This problem corresponds to periodic, counter-rotating vortices whose strength decay in time at a rate determined by the viscosity. The Taylor problem has the analytical solution to the Navier–Stokes equations. The solution is given by [33, 46]

$$u(x, y, t) = \sin(\pi x)\cos(\pi y)\exp(-2\pi^2 t/Re) \tag{33}$$

$$v(x, y, t) = -\cos(\pi x)\sin(\pi y)\exp(-2\pi^2 t/Re) \tag{34}$$

$$p(x, y, t) = 0.25(\cos(2\pi x) + \cos(2\pi y))\exp(-4\pi^2 t/Re) \tag{35}$$

on a square $(0, 0)\leqslant(x, y)\leqslant(1, 1)$ computational domain. The problem is solved by imposing the above time-dependent values of the velocity at the boundary of the domain and introducing its value at $t = 0$ as the initial condition in the domain. The solution should remain unchanged over time in the absence of viscosity. The Reynolds number is defined as $Re = uD/\mu$ where $D = 1.0$ is the domain length scale. The computations were performed for different low and high Reynolds numbers using uniform unstructured meshes. The grid was progressively refined from 8×8 to 32×32 in factors of 2 to verify the overall spatial discretization. As it is known, the flow at lower Reynolds guarantees a fully diffusive behaviour. Therefore, the current formulations approach a second-order accurate scheme in low *Re*. However, the flow at higher Reynolds exhibits a convective-dominated behaviour, hence, the current method reduces to a first-order scheme. Figure 2(a) illustrates the kinetic energy error in terms of the grid resolution. As it is observed, the slopes of the two lines are different for the two low and high Reynolds. It indicates that the spatial accuracy of the current method reduces from lower Reynolds to higher one. Figure 2(b) demonstrates the error *versus* time step. As was mentioned before, the current method would be first-order accurate in time. Following our description provided in Sections 4 and 5, it is worth to reemphasize that the accuracy of the present numerical solutions is excellent in spite of using a first-order method to treat high Reynolds flows even on coarse grid distributions. It is because the use of four inclusive cell-face expressions, see Equations (27)–(28) and (31)–(32), provides a strong coupling between the pressure and velocity fields and minimizes the false diffusion in the domain. This advantage is shown shortly.

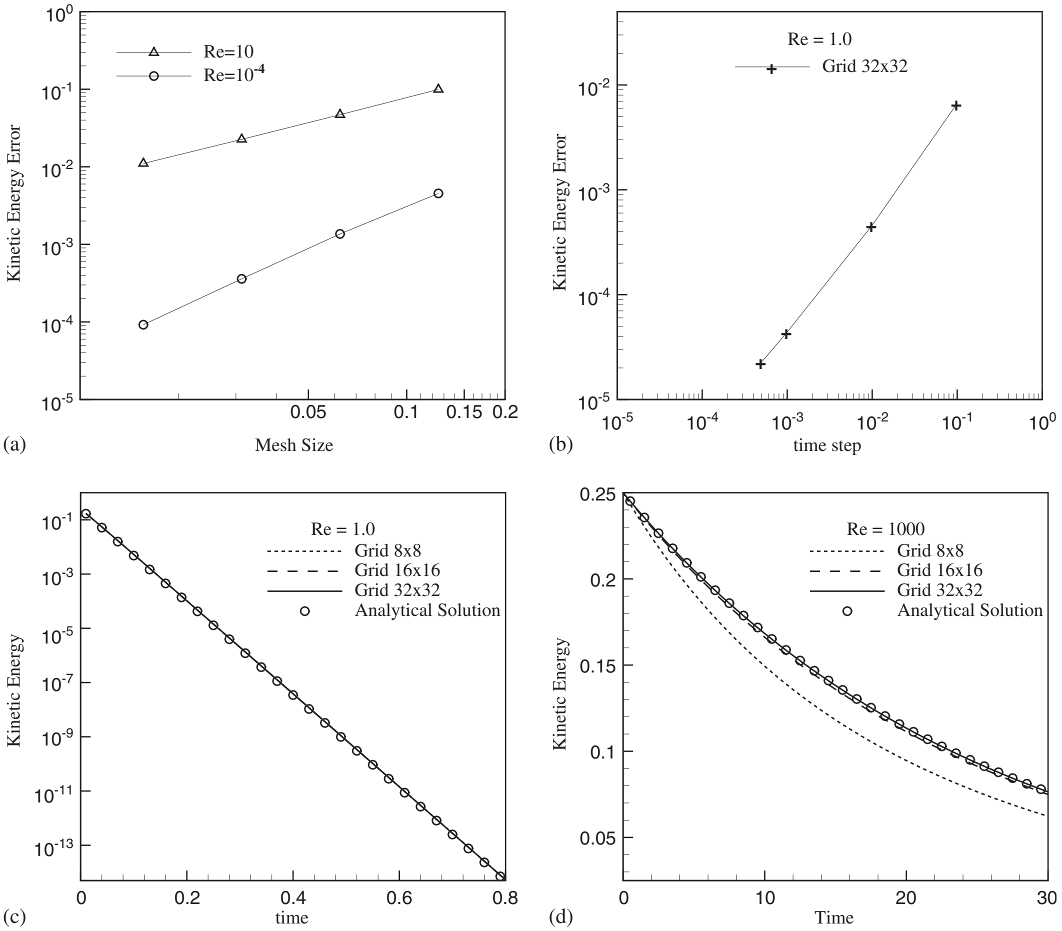

Figure 2. The Taylor problem study and the demonstration of convergence rate *versus* (a) mesh size and (b) time step and the temporal kinetic energy decay at (c) $Re = 1$ and (d) $Re = 1000$.

As was mentioned in the Introduction section, the classical collocated arrangements using the traditional convection schemes may not conserve the global kinetic energy [30–33]. Since the non-staggered schemes may not conserve energy in the discrete sense even for the second-order accurate methods [32], we have chosen the convection of a decaying vortex to check if the energy in the current method is suitably conserved even in inviscid limit. We continue our study on the decaying vortex and consider the two $Re = 1$ and $Re = 1000$ as a fully viscous flow and an approximate inviscid flow limits, respectively. Figures 2(c) and (d) show the decay in kinetic energy as a function of time. Figure 2(c) shows that the kinetic energy is fully conserved even on very coarse grid resolutions. It is because the flow at such low *Re* plays a fully second-order behaviour. Figure 2(d) shows that the kinetic energy is not conserved suitably on coarse grids at $Re = 1000$. As it is seen in this figure, the conservation of kinetic energy on a grid resolution with 32×32 and beyond is guaranteed. Indeed, comparing them with the work of Reference [32], the current global kinetic energy conservation is excellent. Once more, this achievement can be attributed to the advantages of developing inclusive statements at the cell faces of our unstructured volumes.

The second test case is the driven polar cavity taken from Fuchs and Tillmark [67]. The cavity configuration is shown in Figure 3. The cavity is a portion of an annulus with the inner and outer radii of $r=1$ and 2, respectively. The annulus is limited to a circular arc with $-1/2\leqslant\theta\leqslant+1/2$ radians. If U_{r} and U_θ indicate the radial and angular velocity components in a cylindrical coordinate system, all the cavity walls except the bottom one have no-slip boundary conditions, i.e. $U_{\mathrm{r}}=U_\theta=0$. However, the velocity components at the bottom wall are $U_{\mathrm{r}}=0$ and $U_\theta=1$. Furthermore, to complete the boundary condition implementation, one cell in the domain or its boundaries is chosen to fix the pressure field. The investigation is performed at $Re=350$. Figure 3(c) shows the isobars in the polar cavity. The pressure contours are depicted here to pinpoint that the current collocated method does not yield non-physical pressure pattern in the computational domain.

Figures 3(d) and (e) show the current radial and angular velocity profiles along the lines with $\theta=-20$ and 0°. The figures demonstrate the grid-dependent study. In another words, they present the results for three different grid resolutions considering an overall size increase by a factor 4 from one grid to the next fine grid. The coarsest grid with 194 nodes and its next fine grid with 728 nodes are shown in Figures 3(a) and (b), respectively. Figures 3(c) and (d) indicate that the semi-coarse grid shown in Figure 3(b) provides solution with sufficient accuracy. Figure 4 compares the accuracy of the current solution with the experimental data and calculations presented by Fuchs and Tillmark [67] and the calculations presented by Jeng and Chen [34]. Although the current solutions vary slightly from the experimental data, they coincide very closely with the reference's calculations. Similarly, the results of Reference [34] agree well with the current numerical solutions but not with the experimental data provided by Reference [67].

The third test case is the flow in a squeezed cavity. This geometry is obtained by skewing the unit square cavity to the one with an inclination angle of $\beta=45°$. For the boundary condition implementation, zero velocity components are defined at all four walls except the upper lid. The tangential velocity on the upper lid is unity. Additionally, the tangential velocities at the upper corners are also unity; however, no inflow and outflow of mass is allowed between these two nodes and their next neighbouring nodes on the inclined walls. To fix the pressure field, the magnitude of pressure is set zero at the right lower corner. Following Demirdzic *et al.* [68], the study is fulfilled at two Reynolds numbers of 100 and 1000 using two uniform and non-uniform grids. The numbers of boundary nodes are 61×61 for both grids. Figure 5 shows the unstructured grid arrangements for both uniform (top) and non-uniform (bottom) distributions. There are a total of 1994 nodes for the uniform grid and a total of 1813 nodes for the non-uniform grid in their solution domains. The horizontal and vertical velocities are shown in Figures 6(a) and (b) for two Reynolds numbers of 100 and 1000, respectively. The current results are compared with those reported in Reference [68]. Following the reference, the y coordinate for u velocity and the x coordinate for v velocity have been normalized along the centrelines. There is not much difference between the results of two types of grid distributions. The slight differences between the uniform and non-uniform results are due to using almost equal number of nodes in these two grid distributions. If the total number of nodes is not large enough, the local errors on the non-uniform grid become larger than that on the uniform grid. Despite considering this point, the figure shows that the numerical results for both grid arrangements are in excellent agreement and they agree well with the benchmark solutions.

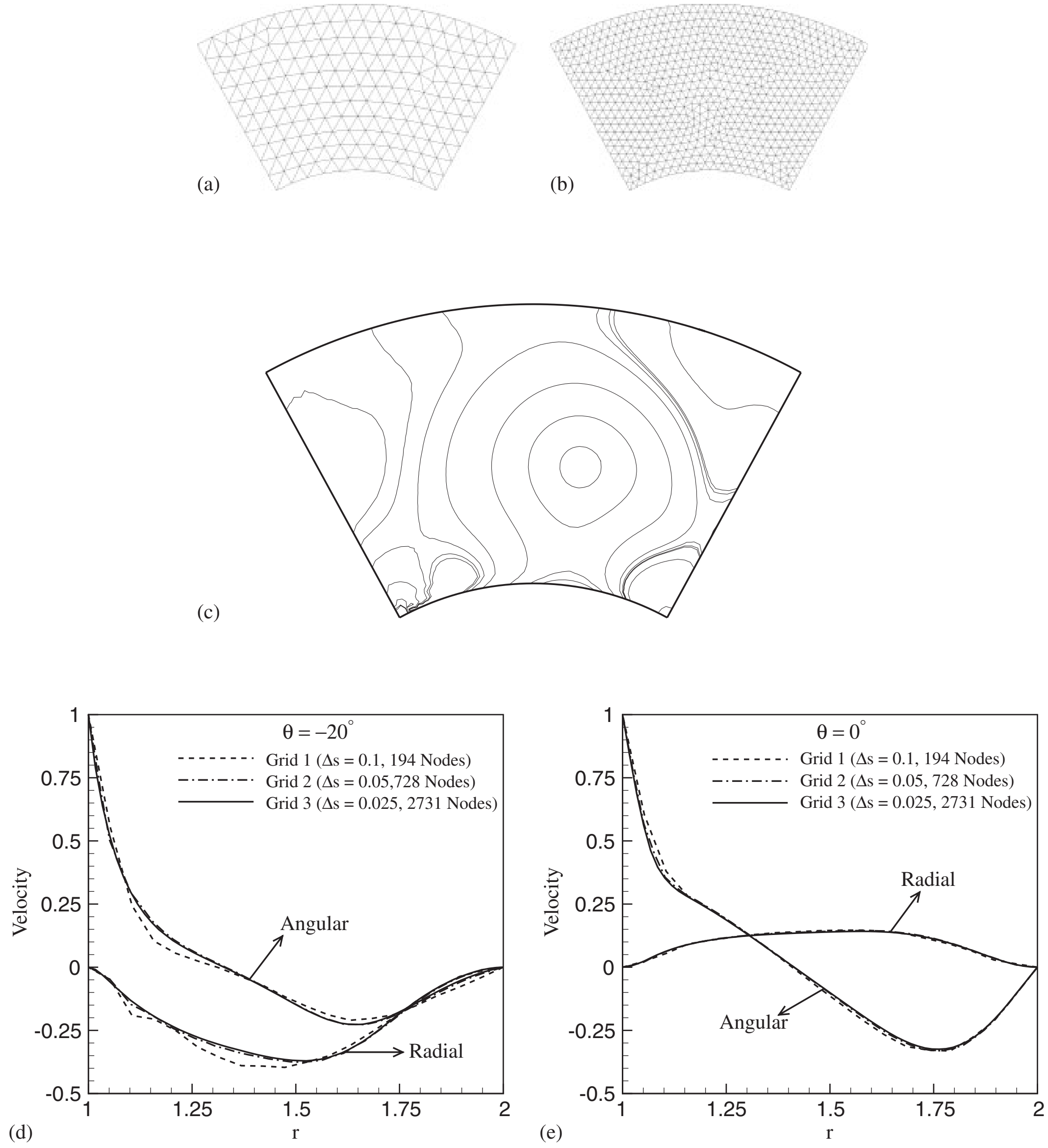

Figure 3. The mesh distributions in polar cavity with (a) 194 nodes and (b) 728 nodes; and the demonstration of (c) pressure contours; and the mesh refinement study for the velocity profiles along (d) $\theta = -20°$ and (e) $\theta = 0°$ radii.

The fourth test case is the flow over a backward-facing step. Based on the flow Reynolds number, several recirculations may appear in the flow field. Armaly *et al*. [69] have presented detailed measurement of velocity distribution and reattachment length for the incompressible flow of air in a 2D channel. The measurement is provided for a wide range of Reynolds numbers from

DOI: 10.1002/fld

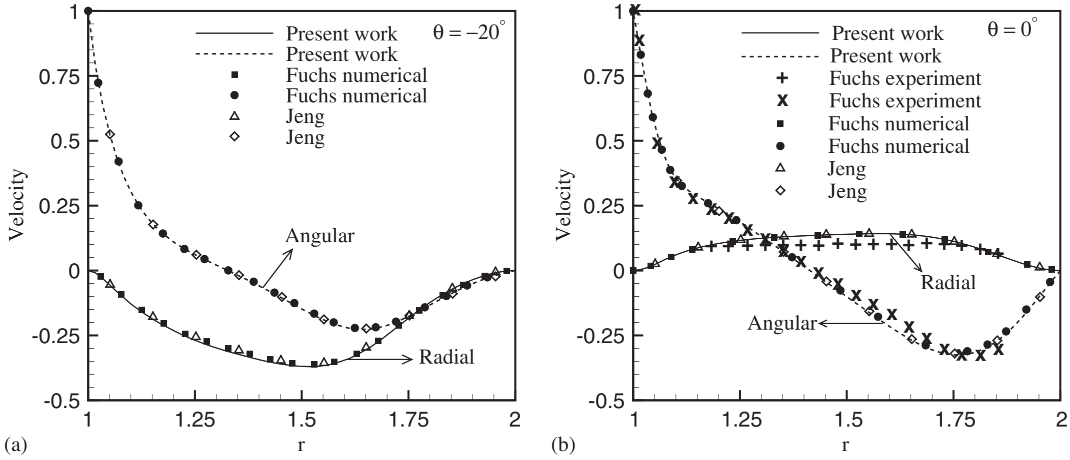

Figure 4. The velocity profiles along: (a) $\theta = -20$ and (b) 0° radii and comparison with the results provided by Fuchs and Tillmark [67] and Jeng and Chen [34].

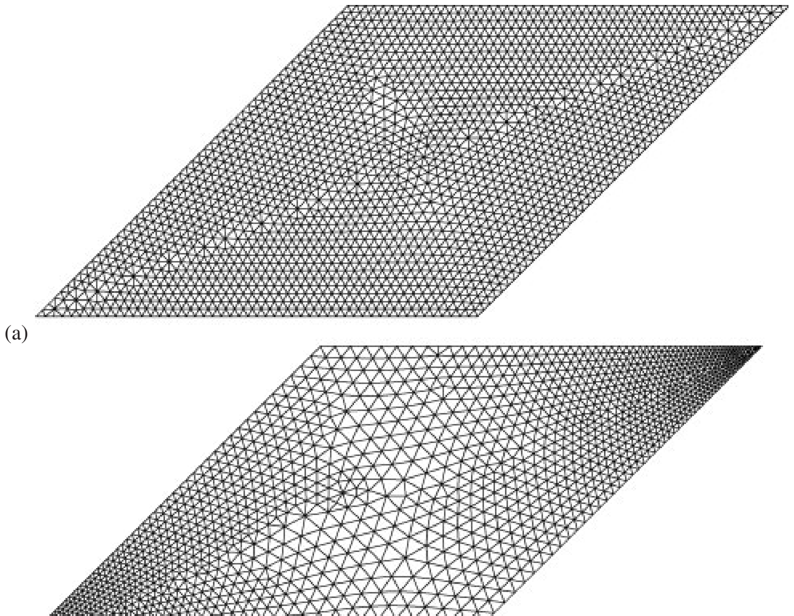

Figure 5. The mesh distributions in the skewed cavity using (a) uniform unstructured grid and (b) non-uniform unstructured grid.

DOI: 10.1002/fld

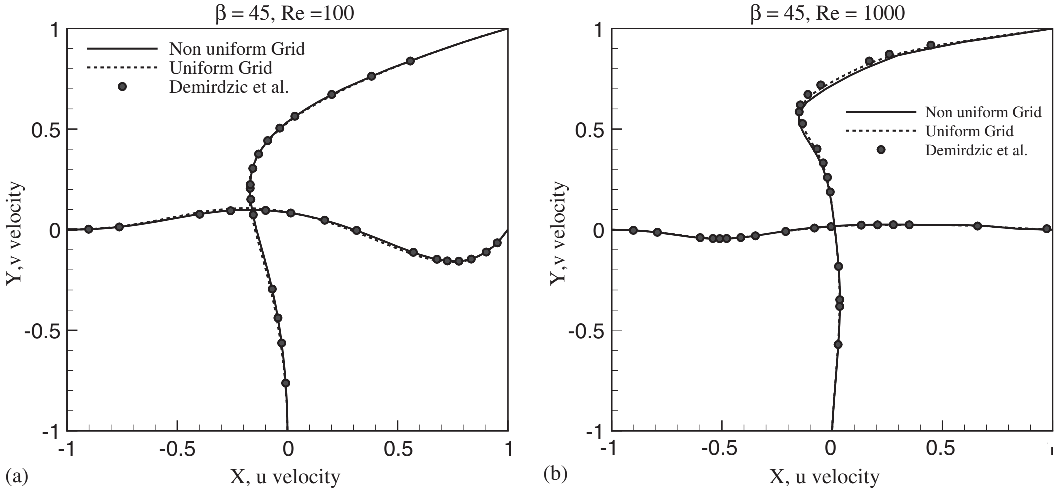

Figure 6. Velocity profiles at the normalized centrelines of the skewed cavity and comparison with those of Demirdzic *et al.* [68]: (a) $Re = 100$; and (b) $Re = 1000$.

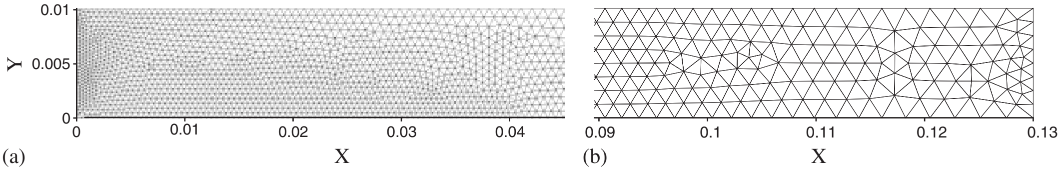

Figure 7. Unstructured grid distribution in the backward-facing step problem: (a) close to step and (b) close to outflow.

70 to 8000. The results show that the various flow regimes are characterized by typical variation of separation length with Reynolds number. We select $Re = 389$ to launch our study because this special Reynolds number has been widely chosen to validate newly developed computational fluid dynamics formulations. The experimental data suggest that the flow with $Re > 400$ generates 3D variation or turbulence in the flow field. The Reynolds number is calculated using twice the height of the inlet channel and two-thirds of the maximum inflow velocity at the step. The numerical computations are performed on both uniform and non-uniform unstructured grid distributions of which the latter one is described here. The grid distribution is observed in Figure 7. The total number of nodes is 1897. Grid is clustered close to the inlet in order to resolve the various viscous gradients and the reattachment point of the separated flow. The choice of non-uniform grid is quite normal in treating the backward-facing step problem [26, 70–72]. It is because the flow is almost fully developed in a major part of the duct downstream of the step. That part does not need fine grid considerations. Following Reference [69], we choose a length-to-height ratio of 13. Darbandi and Vakilipour [72] have extensively investigated the influence of boundary conditions on the accuracy of the numerical calculations. They show that the current formulation can be readily used to solve the same flow field in channels with much shorter lengths without causing adverse effect on the

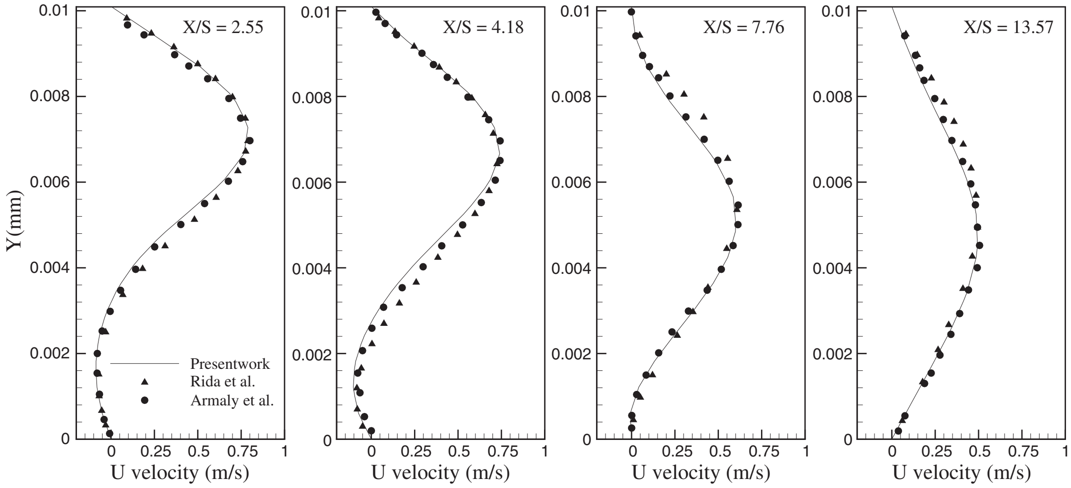

Figure 8. Axial velocity profiles at four longitudinal locations in the backward-facing step problem and comparison with numerical solution of Rida *et al.* [26] and experimental data of Armaly *et al.* [69].

accuracy of the calculations. As before, no slip boundary conditions are used on the walls of the channel and the step itself. A fully developed flow is specified at the inlet. The pressure is fixed at one point but not necessarily at the exit [72].

Figure 8 presents the obtained velocity profiles at four axial locations of $x/s = 2.55$, 4.18, 7.76, and 13.57. The current results are compared with the numerical solution of Rida *et al.* [26] and the experimental data of Reference [69]. Generally speaking, the current results perform better agreement with the experimental data. The unstructured grid of Reference [26] contains 2240 elements. Similar to our grid distribution, their grid is fine close to the inlet and stretched near the outlet. The reference reports a total runtime of 1197 s if the computations are carried out on an IBM RISC 6000 model 340. The reference does not exactly report the chosen convergence criterion magnitude. The total runtimes of the current executions are 818, 1057, 1348, and 1659 s considering different convergence criteria of 1.3×10^{-4}, 1.1×10^{-5}, 1.0×10^{-6}, and 1.1×10^{-7}, respectively.

The next test case is a four-port valve, which can be found in application like fluid network. This test was numerically simulated by Jorgenson and Pletcher [23]. It is a complex geometry to show the versatility of applying boundary conditions when using an unstructured grid flow solver. Following Reference [23], we also solve the problem using compressible formulation. The flow Mach number is 0.05. Figure 9 shows a 2D valve with four ports. Fluid enters through a channel on the left and exits through the bottom channel. A fully developed velocity profile is specified at the inlet. The pressure is specified at the exit. No-slip boundary conditions are applied at all solid walls. Following Reference [23], the problem is tested at two Reynolds of 10 and 50 using compressible formulation. The Reynolds is calculated based on the height of inflow port section and the mean velocity profile at the inlet.

Figure 9(b) depicts the density contours in the domain at $Re = 50$. The density is obtained *via* the equation of state for the air as a perfect gas. At this low Mach number, the density contours mimic isobars. Hence, very similar to isobars given in the polar cavity, see Figure 3(c), no non-physical

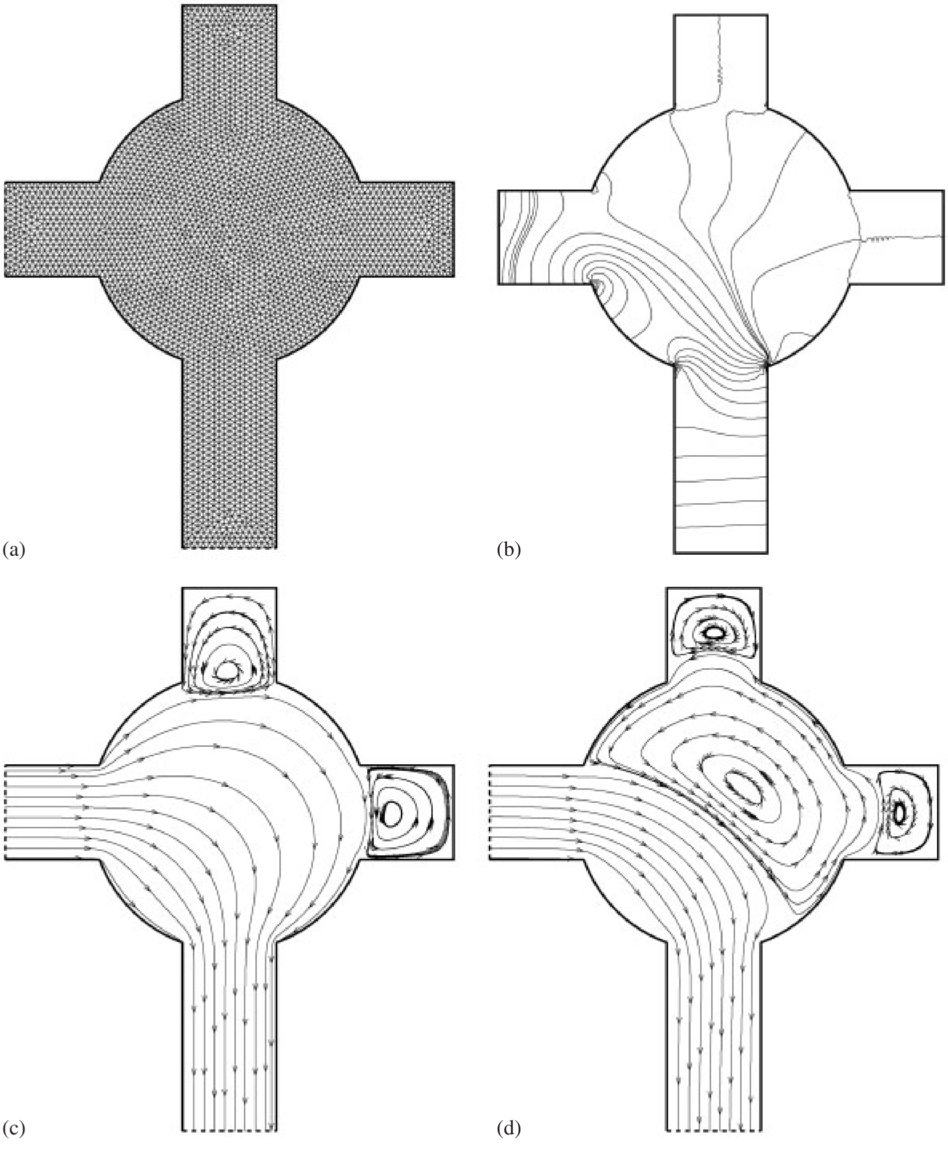

Figure 9. The analysis of flow in a four-port valve: (a) the grid; (b) density contours at $Re = 50$; (c) streamlines at $Re = 10$; and (d) streamlines at $Re = 50$.

oscillatory pattern is observed in four-port valve domain. Figures 9(c) and (d) show the streamlines in the valve at $Re = 10$ and 50, respectively. Schematically, they are in excellent agreement with Reference [23]. As it is seen, the closed valves act as driven cavities. A clockwise rotation of the flow is observed in the central region in $Re = 10$. However, the banded fluid drives a large volume

Table I. The (x, y) locations of the vorticity centres in the four-port valve at two Reynolds and comparison with locations taken from Reference [23].

	Reynolds	Top cavity	Central region	Right cavity
Present work	10	(−0.04, 2.38)	NA	(2.75, −0.03)
Reference [23]	10	(0.00, 2.45)	NA	(2.80, 0.00)
Present work	50	(0.00, 3.05)	(0.52, 0.42)	(3.15, −0.02)
Reference [23]	50	(−0.10, 3.00)	(0.60, 0.35)	(3.25, −0.10)

of fluid in a counterclockwise direction in $Re = 50$. In both cases, the flow redevelops into a fully developed parabolic profiles at the exit.

Although Jorgenson and Pletcher [23] do not quantify their results, there is an opportunity to present an approximate comparison of our predicted vorticity centres with theirs. Table I presents the coordinates of two vorticity centres in the closed ports and one inside the circular region. The current results agree well with those of the reference. It should be noted that the reference does not report the data. We have extracted them from their velocity–vector plots. Therefore, the achieved accuracy is as much as the accuracy presented in their vector plots.

The last test case is the unsteady incompressible flow over a circular cylinder to induce vortex shedding in the wake of high Reynolds flows. The computational domain is confined to boundaries sufficiently far from the cylinder to preclude the undesirable effects of improper boundary locations in the accuracy of our solution. The circular cylinder is of unit diameter with its center located at the origin of the Cartesian coordinates. The dimensions of the far-field region is $[-12.5, 30] \times [-12.5, 12.5]$, see Figure 10(top). The figure shows two far and close views of the generated mesh in the entire domain and in the vicinity of the cylinder, respectively. The computational domain is divided into 4540 unstructured triangular elements using 2332 nodes, which are suitably clustered near the cylinder and its wake. The surface of the cylinder is divided into 42 equal parts. The Dirichlet far-field boundary conditions are applied to the left, bottom, and top outer boundaries considering the free-stream boundary conditions with $u = u_\infty = 1$ and $v = v_\infty = 0$. The right boundary is suitably closed using the advantages of a fully conservative method [72]. The no-slip boundary conditions $u = v = 0$ are implemented at the cylinder surface. Following Williamson [73], the computations were performed at $Re = 100$. Figure 10 presents the streamlines and vorticity contours at a specific time and the vorticity fluctuations at a specific point in the solution domain. In the latter plot, the vorticity magnitude is plotted against time. The periodic behaviour of the flow is fully observed in Figure 10(bottom). Using a normalized time step of 0.1, the shedding period is found to be $T = 6.4$ units, which results in a dimensionless shedding frequency of $St = 0.1562$. Comparing with the experimental measurements of Williamson [73], whose Strouhal number is 0.1643, and the numerical solution of Braza *et al.* [74], whose Strouhal number is 0.16, our shedding frequency shows 4.9 and 2.38% differences with them, respectively. Braza *et al.* employ an alternating-direction-implicit method with a normalized time step of 0.02 in their second-order-accurate finite-volume approach. Considering the use of a first-order accurate formulation in time and a large time step of 0.1, the present accuracy is excellent.

The current computations were carried out on a Pentium III, 550 MHz personal computer. The current experience showed that the current results would not much change if the convergence criterion became less than 10^{-5}.

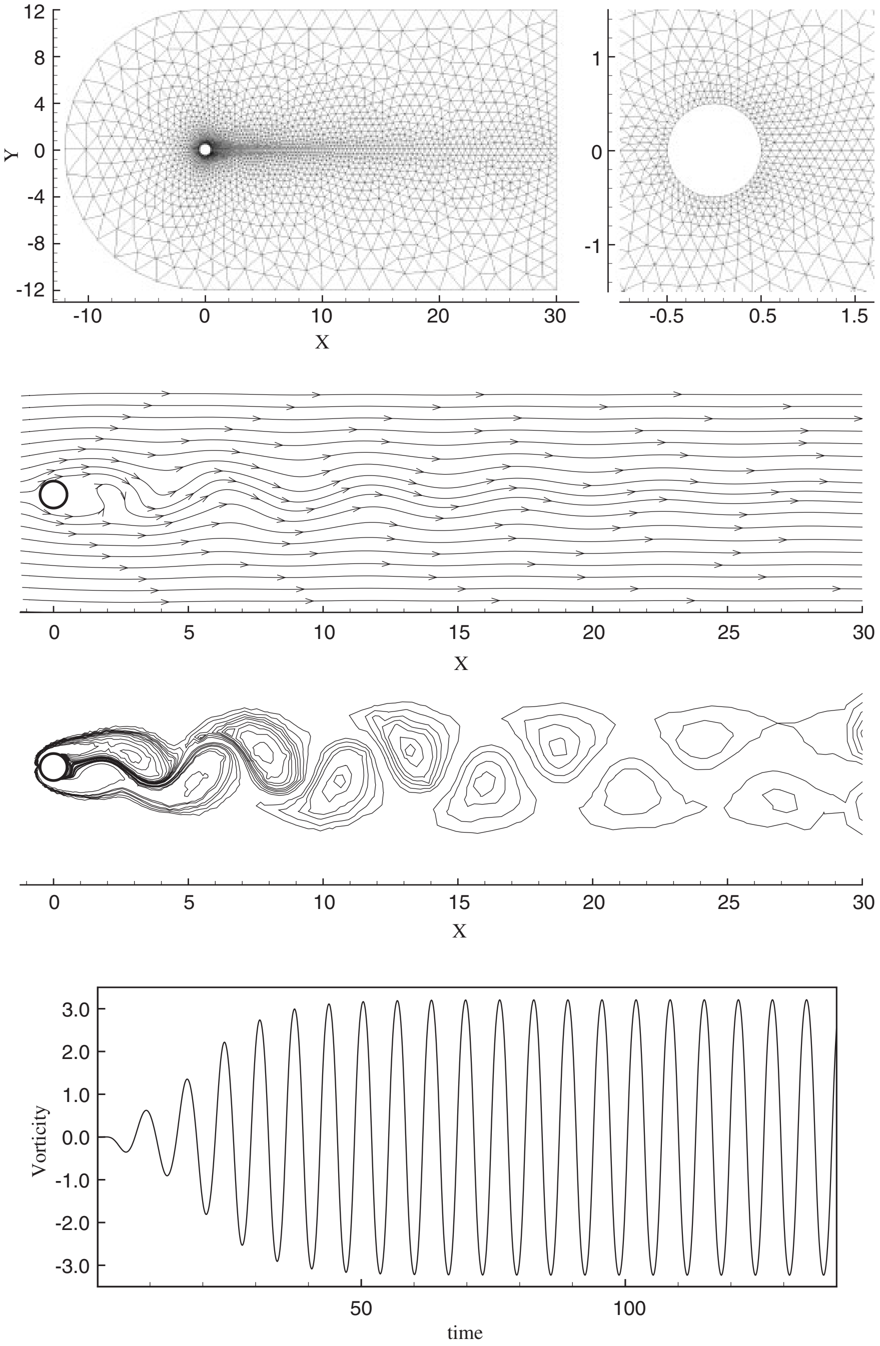

Figure 10. The study of unsteady flow over a cylinder placed in a free stream including mesh, streamlines, vorticity contours, and vorticity fluctuation at an arbitrary node in the domain from top to bottom, respectively, $Re = 100$.

8. CONCLUSION

We extended a pressure-weighted upwinding scheme on collocated unstructured grids benefiting from a hybrid finite-volume element formulation. To consider more physics of flow in our pressure-based formulations, suitable weights of both convection and diffusion physics as well as the pressure influence were incorporated directly in estimating the cell-interface advection. To suppress the non-physical pressure pattern in our solutions, the dual-velocity definition concept was employed and two pairs of momentum component expressions were derived at all cell interfaces. It was shown that the developed formulations would be smart enough to use the second pair of expressions wherever and whenever it deems to be a demand. The comparison of the current solutions with those of benchmark and standard test cases as well as the experimental data showed that the achieved accuracy would be excellent despite using first-order accurate spatial and temporal formulations on very coarse grid resolutions. This can be attributed to the developed pressure-weighted upwinding scheme, which incorporates more effective roles of different terms of the fluid flow governing equations in the cell-interface approximations. The development of the method to unstructured grids has numerously improved the capabilities of the primitive method for solving either the flow in complex geometries or complicated flow fields in simple geometries. The developed formulations and the extended algorithm can be equally utilized to simulate complex incompressible and low-Mach compressible flow fields encountered in engineering applications.

ACKNOWLEDGEMENT

The present work was supported partially by the research center of Sharif University of Technology.

REFERENCES

1. Thompson JF, Soni BK, Weatherill NP. *Handbook of Grid Generation.* CRC Press: Boca Raton, FL, 1998.
2. Mavriplis DJ. Unstructured grid techniques. *Annual Review of Fluid Mechanics* 1997; **29**:473–514.
3. Morgan K, Peraire J. Unstructured grid finite-element methods for fluid mechanics. *Report on Progress in Physics* 1998; **61**:569–638.
4. Lohner R, Morgan K, Peraire J, Vahdati M. Finite element flux-corrected transport (FCT) for the Euler and Navier–Stokes equations. *International Journal for Numerical Methods in Fluids* 1987; **7**:1093–1109.
5. Mavriplis DJ. Accurate multigrid solution of the Euler equations on unstructured and adaptive meshes. *AIAA Journal* 1990; **28**:213–221.
6. Barth TJ. Three-dimensional upwind Euler solver for unstructured meshes. *AIAA Paper 1991-1548*, June 1991.
7. Pironneau O. *Finite Element Methods for Fluids*. Wiley: Chichester, 1989.
8. Zienkiewicz OC, Taylor RL. *The Finite-Element Method* (4th edn), vol. 2. McGraw-Hill: New York, 1991.
9. Farmer J, Martinelli L, Jameson A. A fast multigrid method for solving incompressible hydrodynamics problems with free surfaces. *AIAA Paper 1993-0767*, 1993.
10. Peraire J, Morgan K, Perio J. The simulation of 3D incompressible flows using unstructured grids. In *Frontiers of Computational Fluid Dynamics 1994*, Caughey DA, Hafez MM (eds). Wiley: New York, 1994; 281–301.
11. Anderson WK, Rausch RD, Bonhaus DL. Implicit/multigrid algorithms for incompressible turbulent flows on unstructured grids. *Journal of Computational Physics* 1996; **128**:391–408.
12. Wang Q, Joshi Y. Algebraic multigrid preconditioning for fluid flow and heat transfer on unstructured meshes. *Numerical Heat Transfer*, *Part B* 2006; **49**:197–221.
13. Barth TJ, Jepersen DC. The design and application of upwind schemes on unstructured meshes. *AIAA Paper 89-0366*, 1989.
14. Zhao Y, Zhang B. A high-order characteristic upwind FV method for incompressible flow and heat transfer simulation on unstructured grids. *Computer Methods in Applied Mechanics and Engineering* 2000; **190**:733–756.

15. Woodfield PL, Suzuki K, Nakabe K. A simple strategy for constructing bounded convection schemes for unstructured grids. *International Journal for Numerical Methods in Fluids* 2004; **46**:1007–1024.
16. Raithby GD. A critical evaluation of upstream differencing applied to problems involving fluid flow. *Computer Methods in Applied Mechanics and Engineering* 1976; **9**:75–103.
17. Raithby GD. Skew upstream differencing schemes for problems involving fluid flow. *Computer Methods in Applied Mechanics and Engineering* 1976; **9**:153–164.
18. Schneider GE, Raw MJ. A skewed, positive influence coefficient upwinding procedure for control-volume-based finite-element convection-diffusion computation. *Numerical Heat Transfer* 1986; **9**:1–26.
19. Schneider GE, Raw MJ. Control volume finite-element method for heat transfer and fluid flow using collocated variables. *Numerical Heat Transfer* 1987; **11**:363–390.
20. Darbandi M, Schneider GE. Analogy-based method for solving compressible and incompressible flows. *Journal of Thermophysics and Heat Transfer* 1998; **12**:239–247.
21. Chorin AJ. A numerical method for solving incompressible viscous flow problems. *Journal of Computational Physics* 1967; **2**:12–26.
22. Ekaterinaris JA. High-order accurate numerical solutions of incompressible flows with the artificial compressibility method. *International Journal for Numerical Methods in Fluids* 2004; **45**:1187–1207.
23. Jorgenson PCE, Pletcher RH. An implicit numerical scheme for the simulation of internal viscous flow on unstructured grids. *Computers & Fluids* 1996; **25**:447–466.
24. Harlow FH, Welch JE. Numerical calculation of time dependent viscous incompressible flow of fluid with free surface. *Physics of Fluids* 1965; **8**:2182–2189.
25. Shih TM, Tan CH, Hwang BC. Effects of grid staggering on numerical schemes. *International Journal for Numerical Methods in Fluids* 1989; **9**:193–212.
26. Rida S, McKenty F, Meng FL, Reggio M. A staggered control volume scheme for unstructured triangular grids. *International Journal for Numerical Methods in Fluids* 1997; **25**:697–717.
27. Kobayashi MH, Pereira JMC, Pereira JCF. A conservative finite-volume second-order-accurate projection method on hybrid unstructured grids. *Journal of Computational Physics* 1999; **150**:40–75.
28. Vidovic D, Segal A, Wesseling P. A superlinearly finite volume method for the incompressible Navier–Stokes equations on staggered unstructured grids. *Journal of Computational Physics* 2004; **198**:159–177.
29. Baliga BR, Patankar SV. A control-volume finite-element method for two dimensional fluid flow and heat transfer. *Numerical Heat Transfer* 1983; **6**:245–261.
30. Perot B. Conservation properties of unstructured staggered mesh schemes. *Journal of Computational Physics* 2000; **159**:58–89.
31. Zhang X, Schmidt D, Perot B. Accuracy and conservation properties of a three-dimensional unstructured staggered mesh scheme for fluid dynamics. *Journal of Computational Physics* 2002; **175**:764–791.
32. Benhamadouche S, Laurence D. Global kinetic energy conservation with unstructured meshes. *International Journal for Numerical Methods in Fluids* 2002; **40**:561–571.
33. Mahesh K, Constantinescu G, Moin P. A numerical method for large-eddy simulation in complex geometries. *Journal of Computational Physics* 2004; **197**:215–240.
34. Jeng YN, Chen JL. Geometric conservation law of the finite volume method for the SIMPLER algorithm and a proposed upwind scheme. *Numerical Heat Transfer*, *Part B* 1992; **22**:211–234.
35. Darbandi M, Zakyani M. Solving turbulent flow in curvilinear coordinate system using covariant velocity calculation procedure. In *Computational Methods*, Liu *et al.* (eds). Springer: The Netherlands, 2006; 161–175.
36. Shyy W, Vu TC. On the adoption of velocity variable and grid system for fluid flow computation on curvilinear coordinates. *Journal of Computational Physics* 1991; **92**:82–105.
37. Peric M, Kessler R, Scheuerer G. Comparison of finite-volume numerical methods with staggered and collocated grids. *Computer & Fluids* 1988; **16**:389–403.
38. Rhie CM, Chow WL. Numerical study of the turbulent flow past an airfoil with trailing edge separation. *AIAA Journal* 1983; **21**:1525–1532.
39. Prakash C, Patankar SV. A control-volume based finite-element method for solving the Navier–Stokes equations using equal-order velocity–pressure interpolation. *Numerical Heat Transfer* 1986; **9**:253–276.
40. Saabas HJ, Baliga BR. Co-located equal-order control-volume finite-element method for multidimensional, incompressible, fluid flow—Part I. *Numerical Heat Transfer*, *Part B* 1994; **26**:381–407.
41. Masson C, Saabas HJ, Baliga BR. Co-located equal-order finite-volume finite-element method for two-dimensional axisymmetric incompressible fluid flow. *International Journal for Numerical Methods in Fluids* 1994; **18**:1–26.
42. Tran LD, Masson C, Smaili A. A stable second-order mass-weighted upwind scheme for unstructured meshes. *International Journal for Numerical Methods in Fluids* 2006; **51**:749–771.

DOI: 10.1002/fld

43. Davidson L. A pressure correction method for unstructured meshes with arbitrary control volumes. *International Journal for Numerical Methods in Fluids* 1996; **22**:265–281.
44. Lai YG. Unstructured grid arbitrarily shaped element method for fluid flow simulation. *AIAA Journal* 2000; **38**:2246–2252.
45. Issa RI. Solution of the implicitly discretized fluid flow equations by operator-splitting. *Journal of Computational Physics* 1986; **62**:40–65.
46. Chenier E, Eymard R, Touazi O. Numerical results using a colocated finite-volume scheme on unstructured grids for incompressible fluid flows. *Numerical Heat Transfer*, *Part B* 2006; **49**:259–276.
47. Darbandi M, Schneider GE. Momentum variable procedure for solving compressible and incompressible flows. *AIAA Journal* 1997; **35**:1801–1805.
48. Darbandi M, Schneider GE, Javadi K, Solhpour N. The performance of a physical influence scheme in structured triangular grids. *AIAA Paper 2003-0436*, Reno, Nevada, January 2003.
49. Darbandi M, Naderi AR. Multiblock hybrid grid finite volume method to solve flow in irregular geometries. *Computer Methods in Applied Mechanics and Engineering* 2006; **196**:321–336.
50. McGuirk JJ, Page GJ. Shock capturing using a pressure-correction method. *AIAA Journal* 1990; **28**:1751–1757.
51. Darbandi M, Hosseinizadeh SF. General pressure-correction strategy to include density variation in incompressible algorithms. *Journal of Thermophysics and Heat Transfer* 2003; **17**:372–380.
52. Darbandi M, Schneider GE. Comparison of pressure-based velocity and momentum procedures for shock tube problem. *Numerical Heat Transfer*, *Part B* 1998; **33**:287–300.
53. Darbandi M, Schneider GE. Performance of an analogy-based all-speed procedure without any explicit damping. *Computational Mechanics* 2000; **26**:459–469.
54. Darbandi M, Mokarizadeh V. A modified pressure-based algorithm to solve the flow fields with shock and expansion waves. *Numerical Heat Transfer*, *Part B* 2004; **46**:497–504.
55. Darbandi M, Roohi E, Mokarizadeh V. Conceptual linearization of Euler governing equations to solve high speed compressible flow using a pressure-based method. *Numerical Methods for Partial Differential Equations* 2007, in press.
56. Darbandi M, Schneider GE. Thermobuoyancy treatment for electronic packaging using an improved advection scheme. *ASME Journal of Electronic Packaging* 2003; **125**:244–250.
57. Sani RL, Gresho PM, Lee RL, Griffiths DF. The cause and cure of the spurious pressures generated by certain F.E.M. solutions of the incompressible Navier–Stokes equations Part 1 and Part 2. *International Journal for Numerical Methods in Fluids* 1981; **1**:17–43, 171–204.
58. Gunzburger MD. *Finite Element Methods for Viscous Incompressible Flows*. Academic Press: Boston, MA, 1989.
59. Thomasset S. *Implementation of Finite Elements for the Navier–Stokes Equations*. Springer: Berlin, 1981.
60. Fernandez G, Hafez M. Stable finite-element solution of the incompressible Navier–Stokes equations using linear interpolations for velocity and pressure. *Computer Methods in Applied Mechanics and Engineering* 2001; **191**:545–559.
61. Versteeg HK, Malalasekera W. *An Introduction to Computational Fluid Dynamics*. *The Finite Volume Method*. Addison-Wesley/Longman Limited: Reading/New York, 1995.
62. Darbandi M, Bostandoost SM. A new formulation toward unifying the velocity role in collocated variable arrangement. *Numerical Heat Transfer*, *Part B* 2005; **47**:361–382.
63. Duff IS, Erisman AM, Reid JK. *Direct Methods for Sparse Matrices*. Oxford University Press: Oxford, 1992.
64. Darbandi M, Schneider GE, Vakili S. Using different preconditioned Krylov subspace methods to solve coupled fluid flow equations. *CFD Journal* 2006; **15**:35–43.
65. Darbandi M, Banaeizadeh A. Parallel computation of the Navier–Stokes equations using implicit finite volume method. *Proceedings of the 4th European Congress on Computational Methods in Applied Sciences and Engineering*, *ECCOMAS 2004*, Jyvaskyla, Finland, 24–28 July 2004.
66. Darbandi M, Schneider GE, Bostandoost SM. Parallel computation of a fully implicit finite volume method using different ordering strategies. *AIAA Paper 2004-0994*, 5–8 January 2004.
67. Fuchs L, Tillmark N. Numerical and experimental study of driven flow in a polar cavity. *International Journal for Numerical Methods in Fluids* 1985; **52**:311–329.
68. Demirdzic I, Lilek Z, Peric M. Fluid flow and heat transfer problems for non-orthogonal grids: benchmark solutions. *International Journal for Numerical Methods in Fluids* 1992; **15**:329–354.
69. Armaly BF, Durst F, Pereira JCF, Schonung B. Experimental and theoretical investigation of backward-facing step flow. *Journal of Fluid Mechanics* 1983; **127**:473–496.
70. Gartling DK. A test problem for outflow boundary conditions-flow over a backward-facing step. *International Journal for Numerical Methods in Fluids* 1990; **11**:953–967.

DOI: 10.1002/fld

71. Darbandi M, Schneider GE. Application of an all-speed flow algorithm to heat transfer problems. *Numerical Heat Transfer*, *Part A* 1999; **35**:695–715.
72. Darbandi M, Vakilipour S. Using fully implicit conservative statements to close open boundaries passing through recirculations. *International Journal for Numerical Methods in Fluids* 2007; **53**:371–389.
73. Williamson CHK. Oblique and parallel modes of vortex shedding in the wake of a circular cylinder at low Reynolds numbers. *Journal of Fluid Mechanics* 1989; **206**:579–628.
74. Braza M, Chassaing P, Ha Minh H. Numerical study and physical analysis of the pressure and velocity fields in the near wake of a circular cylinder. *Journal of Fluid Mechanics* 1986; **165**:79–130.